

A Mid-infrared Study of Superluminous Supernovae

Luming Sun^{1*}, Lin Xiao^{2,3}, and Ge Li⁴

¹*Department of Physics, Anhui Normal University, Jiuhe Road 189, Wuhu 241002, China*

²*Department of Physics, College of Physical Sciences and Technology, Hebei University, Wusidong Road 180, Baoding 071002, China*

³*Key Laboratory of High-precision Computation and Application of Quantum Field Theory of Hebei Province, Hebei University, Wusidong Road 180, 071002, Baoding, China*

⁴*Department of Modern Physics, University of Science and Technology of China, Hefei 230026, China*

Accepted XXX. Received YYY; in original form ZZZ

ABSTRACT

We present the mid-infrared (MIR) light curves (LC) of 10 superluminous supernovae (SLSNe) at $z < 0.12$ based on WISE data at 3.4 and 4.6 μm . Three of them, including PS15br, SN 2017ens, and SN 2017err show rebrightening which started at 200–400 days and ended at 600–1000 days, indicating the presence of dust. In four of the left seven SLSNe, dust emission was detected with monochromatic luminosities of $10^7 \sim 10^8 L_{\odot}$ at epochs of 100–500 days based on MIR colors $W1 - W2 \sim 1$. Among the three SLSNe which show rebrightening, we further analysed PS15br and SN 2017ens. We modeled the SEDs at 500–700 days, which gives dust temperatures of 600–1100 K, dust masses of $\gtrsim 10^{-2} M_{\odot}$, and luminosities of $10^8 \sim 10^9 L_{\odot}$. Considering the time delay and the huge amount of energy released, the emitting dust can hardly be pre-existing dust heated whether collisionally by shocks or radiatively by peak SLSN luminosity or shock emission. Instead, it can be newly formed dust additionally heated by the interaction of circum-stellar medium, indicated by features in their spectra and slowly declining bolometric LCs. The dust masses appear to be ten times greater than those formed in normal core-collapse supernovae at similar epochs. Combining with the analysis of SN 2018bsz by Chen et al. (2022), we suggest that SLSNe have higher dust formation efficiency, although future observations are required to reach a final conclusion.

Key words: supernovae: general – supernovae: individual: PS15br – supernovae: individual: SN 2017ens

1 INTRODUCTION

Superluminous supernovae (SLSNe Gal-Yam 2012, 2019) are a group of supernovae (SNe) with peak luminosities tens or hundreds higher than those of normal SNe. They are so rare that only ~ 100 cases have been discovered. SLSNe usually take longer to rise and decay than normal SNe: they take one to two months to reach their maximum light after explosion, and take about half a year or longer to evolve into a nebular phase or disappear. SLSNe can be classified into two types according to their near-peak optical spectra: Superluminous Supernovae I (SLSN-I) with no hydrogen lines, and Superluminous Supernovae II (SLSN-II) with hydrogen lines. SLSN-I show a blue continuum with weak oxygen and carbon absorption features near the peak time, and show spectra resemble those of SN-Ic in the late time. SLSN-II show hydrogen and helium broad emission lines, and some of them also show narrow emission lines and hence can be called SLSN-II_n. The energy sources of SLSNe have not been well understood (see Sukhbold & Woosley 2016, for a review). The models of the energy sources include pair-instability supernovae (e.g., Gal-Yam et al. 2009), newly born magnetars (e.g., Quimby et al. 2011), circum-stellar medium (CSM) interactions (e.g.,

Smith et al. 2007), and some others. Although the mechanism of SLSNe is still uncertain, SLSNe are generally associated with the explosions of massive stars, or even the most massive stars. In addition, nearby SLSNe often reside in galaxies with low mass and low metallicity (e.g., Perley et al. 2016). The SLSN progenitors and hosts are reminiscent of the first generation of stars and galaxies in the early universe (Gal-Yam et al. 2009). And hence SLSNe might be more common at high redshift than they are now.

Some SLSNe emit in the infrared (IR) band. From most of SLSNe, the IR emission drops along with their optical emission and can be interpreted as emission from the cooling SLSN photosphere. While a few SLSNe, which we will enumerate later, show IR excess relative to the expected level of photospheric emission. SN 2006gy, the first well-studied case of SLSN-II_n, showed a near-infrared (NIR) excess possibly starting around +130d (after explosion), rising before +400d, dropping after +700d, and even being detected around +3000d (Smith et al. 2008; Miller et al. 2010; Fox et al. 2015). Another SLSN-II with no narrow lines, SN 2008es, also showed NIR excess on +254d and +301d (after explosion) (Bhrombhakdi et al. 2019). The closest SLSN-I to date, SN 2018bsz, showed a NIR excess from +232d (after peak) to +265d (Chen et al. 2022). A follow-up mid-infrared (MIR)

* E-mail: sunluming@ahnu.edu.cn

monitoring revealed an MIR excess which begins from +265d at the latest and can still be detected up to +535d.

These IR excesses were generally interpreted as emissions from dust around the SLSNe. However, these works have reached different conclusions about the origin of dust. [Miller et al. \(2010\)](#) interpreted the NIR excess in SN 2006gy between +400d and +700d as a light echo from a massive ($\gtrsim 10 M_{\odot}$) dusty shell heated by the SN peak luminosity. [Fox et al. \(2015\)](#) argued that the NIR excess in SN 2006gy at about +3000d is not an echo, but an emission from dust that is radiatively heated by late-time CSM interaction. [Bhrombhakdi et al. \(2019\)](#) interpreted the NIR excess in SN 2008es as emission from newly formed dust. An important basis for their conclusion is that the H α emission line changes from a symmetric profile in the early time (+89d) to a blue-skewed profile in the late time (+288d). The variation in the H α profile is consistent with a scenario that the condensing dust preferentially obscures the emission in the far side (e.g., [Smith et al. 2009](#)). [Chen et al. \(2022\)](#) demonstrated that the IR excess in SN 2018bsz is difficult to explain by an echo by analysing multi-band monitoring data. They found that the IR excess can otherwise be interpreted as emission from newly formed dust, and estimated the dust mass to be 10^{-4} to $10^{-2} M_{\odot}$ between +265d and +535d. In brief, the dust origin in SLSNe has not been definitively concluded and requires further investigation.

Similarly, the dust origin in most normal SNe remains unclear as the emitting dust can be either pre-existing or newly formed (e.g., [Fox et al. 2011](#); [Szalai & Vinko 2013](#); [Tinyanot et al. 2016](#); [Szalai et al. 2019, 2021](#)). This ambiguity hinders further research on some important topics, such as the mass loss of the SN progenitor for the case of pre-existing dust and the dust formation efficiency for the case of newly formed dust. The same goes for SLSNe. MIR observations are usually more useful for constraining the dust properties than NIR observations (e.g., [Fox et al. 2011](#)). Thus we aim for a comprehensive study of the MIR properties of SLSNe, which are still poorly understood.

The Spitzer Space Telescope and the Wide field Infrared Survey Explorer (WISE) telescope ([Wright et al. 2010](#)) are powerful tools for MIR astronomy. Most MIR studies of SNe were based on Spitzer data, because of the great spatial resolution (1.6'' in I1 and I2 bands) and the high sensitivity (5σ detection limit $I1 = 19.9$ and $I2 = 18.7$ with 100-seconds exposure) of the instrument. While a few MIR studies have used WISE data (e.g., [Prieto et al. 2012](#); [Fox et al. 2013](#); [Kokubo et al. 2019](#); [Tartaglia et al. 2020](#); [Moriya et al. 2020](#)). The WISE telescope has been conducting repetitive all-sky surveys since 2010. The surveys with the telescope include the initial WISE survey, the NEOWISE survey in 2010 and 2011 ([Mainzer et al. 2011](#)), and the NEOWISE-R survey restarted in 2014 after a hiatus between 2011 and 2013 ([Mainzer et al. 2014](#)). The strategy of the surveys results in a regular cadence: a typical target is visited by the telescope every half a year (except for the hiatus), and during each visit 8–25 exposures were taken. Initially, 4 filters were used, and after the cryogen was exhausted in September 2010, only two filters with central wavelengths of 3.4 and 4.6 μm , named W1 and W2 respectively, were used. The 5σ detection limits are $W1 = 15.8$ and $W2 = 14.4$ on a single-exposure image with a typical exposure time of ~ 9 seconds. If interested in events with variability time scales of months to years and careless

about any intra-day variability, one can obtain time-resolved coadded (TRC) images by stacking the single-exposure images taken during each WISE visit ([Meisner et al. 2018](#)). The detection limits on the TRC images are ~ 1.3 magnitudes fainter than on the single-exposure images. Compared with Spitzer, WISE is inferior in spatial resolution (6.1'' and 6.6'' in the W1 and W2 bands) and depth, but superior in sample size and monitoring duration. Thus WISE data is suitable for the study of rare and bright SNe, such as SLSNe.

In this work, we studied the MIR emission of a sample of nearby SLSNe occurred in recent years using WISE data. Throughout the paper, we adopted cosmological parameters of $H_0 = 69.6 \text{ km s}^{-1} \text{ Mpc}^{-1}$, $\Omega_m = 0.286$ and $\Omega_{\Gamma} = 0.714$ from [Planck Collaboration et al. \(2016\)](#).

2 SAMPLE SELECTION AND MIR PHOTOMETRIES

2.1 Sample Selection

We selected a sample of nearby SLSNe from Open Supernova Catalog (OSC, [Guillochon et al. 2017](#)) and the Weizmann Interactive Supernova Data Repository (WiSeREP, [Yaron & Gal-Yam 2012](#)) with four selection criteria as follows. Firstly, the SN has a peak absolute magnitude < -21 ([Gal-Yam 2012](#)). Secondly, the SLSN exploded between 2015 and 2018, so the NEOWISE-R observation spans from the explosion to years after the optical peak. Thirdly, the SLSN has a redshift < 0.12 , and hence the 3σ detection limits on WISE TRC images ($W1 \sim 17.6$ mag and $W2 \sim 16.2$ mag) correspond to monochromatic luminosities (λL_{λ}) at 3.4 and 4.6 μm of $\lesssim 10^{8.5} L_{\odot}$. Finally, the SLSN was spectroscopically classified with certainty. Note that we not only required a distinction between SLSN-I and SLSN-II, but also required that it was not considered to be a tidal disruption event (TDE), and hence SN 2016ezh (=PS16dtm, [Blanchard et al. 2017](#)) was excluded.

The final sample includes 11 SLSNe. We collected the basic information of the SLSNe, including the spectral type, the time of optical peak (t_{peak}), the redshift, and the position, from the literature. We did not find the t_{peak} for LSQ15abl and SN 2017err from the literature, thus we estimated the t_{peak} for LSQ15abl using archival data and obtained the t_{peak} for SN 2017err via private communication (see details in Appendix A). The information is listed in Tab. 1. The sample includes 8 SLSN-I and 3 SLSN-II. Note that SN2017ens, which we have classified as SLSN-I, is special in that its spectrum was type I around the peak and became type II_n in the late time ([Chen et al. 2018](#)). Throughout this paper, we calculated the phases using the time of optical peak as the zero point, because we lack information on the time of explosion for most SLSNe in the sample.

2.2 MIR Photometries

We made MIR photometries of the SLSNe using the WISE TRC images produced by [Meisner et al. \(2018\)](#). There are 16 or 17 available images of each SLSN position in each of the W1 and W2 bands: the first two or three were taken between 2010 and 2011, and the remaining 14 were taken between 2014 and 2020. For each SLSN, we created a reference image

Table 1. Information of the SLSNe sample.

Name	Type	optical peak	z	RA	DEC	Ref
PS15br	SLSN-II	2015 Mar 8 (57089.3)	0.101	11:25:19.22	+08:14:18.9	1
SN 2015bn	SLSN-I	2015 Mar 21 (57102.0)	0.1136	11:33:41.55	+00:43:33.4	2
LSQ15abl	SLSN-II	2015 Apr 24 (57136)	0.087	09:40:29.50	-04:11:32.3	3
SN 2016eay	SLSN-I	2016 Jun 2 (57541.4)	0.1013	12:02:51.71	+44:15:27.4	4,5
SN 2017ens	SLSN-I	2017 Jun 20 (57924.0)	0.1086	12:04:09.37	-01:55:52.2	6
SN 2017egm	SLSN-I	2017 Jun 21 (57925.8)	0.0307	10:19:05.62	+46:27:14.1	7
SN 2017err	SLSN-II _n	2017 Jul 1 (57935)	0.107	11:11:25.10	+00:06:58.5	8
SN 2017gci	SLSN-I	2017 Aug 25 (57990.3)	0.0873	06:46:45.02	-27:14:55.8	9
SN 2018bgv	SLSN-I	2018 May 15 (58253.2)	0.0795	11:02:30.29	+55:35:55.8	10
SN 2018bsz	SLSN-I	2018 May 29 (58267.5)	0.0267	16:09:39.11	-32:03:45.6	11
SN 2018hti	SLSN-I	2018 Dec 12 (58464.6)	0.0612	03:40:53.75	+11:46:37.3	12

The references are: (1) [Inserra et al. \(2018\)](#); (2) [Nicholl et al. \(2016\)](#); (3) [Prajs et al. \(2015\)](#); (4) [Yan et al. \(2017\)](#); (5) [Nicholl et al. \(2017\)](#); (6) [Chen et al. \(2018\)](#); (7) [Bose et al. \(2018\)](#); (8) [Chen et al. \(2017\)](#); (9) [Fiore et al. \(2021\)](#); (10) [Lunnan et al. \(2020\)](#); (11) [Anderson et al. \(2018\)](#); (12) [Lin et al. \(2020\)](#).

in each band by combining the pre-explosion images using SWarp ([Bertin 2010](#)). Here the pre-explosion images refer to images taken at least 60 days before the optical peak, and there are 4–12 pre-explosion images for each SLSN. For all the post-explosion images, we performed image subtraction with ISIS (version 2.2, [Alard & Lupton 1998](#); [Alard 2000](#)). We display the pre-explosion, post-explosion, and difference images in Appendix B.

We performed PSF-fitting photometry to the SLSNe on the difference images using a method described in [Lang et al. \(2016\)](#). When fitting with PSF, the positions of the targets were fixed on the SLSN positions from optical surveys. For most of the SLSNe, the host galaxy is weak and we measured the error through standard procedures. The host galaxies of LSQ15abl, SN 2017egm, and SN 2018bsz are bright and introduce an extra error. The extra error can lead to false detections on reference-subtracted pre-explosion images. Therefore we estimated the extra error using the root square mean of the fluxes of the false detections and added it to the total error. We list all the photometries in Appendix B. We set a 3σ threshold for a detection and calculated a 3σ upper limit when there is no detection.

SN 2018bsz, an SLSNe in the sample, was also observed by Spitzer in I1 and I2 bands. We found that the fluxes of SN 2018bsz measured by WISE and Spitzer are in agreement, as can be seen in detail in Appendix C. This supports the reliability of studying SLSNe using WISE data.

3 DATA ANALYSIS AND RESULTS

3.1 MIR Light Curves

MIR emission was detected from 10 out of 11 SLSNe, and the only exception is SN 2018bgv. Fig. 1 shows the light curves in W1 and W2 bands (expressed as λL_λ) of the 10 SLSNe. SN 2017egm, SN 2018bsz, and SN 2018hti, the three closest SLSNe ($z < 0.07$) in the sample, show a similar pattern in the MIR LCs. Their MIR emission peaks between 0d and +100d with a monochromatic luminosity of $\sim 10^8 L_\odot$, then decreases continuously, and finally fades between +400d and +500d. Limited by large measurement errors, we cannot clearly tell the shape of the LCs of SN 2015bn, LSQ15abl, SN 2016eay, and SN 2017gci. Nonetheless, an assumption that

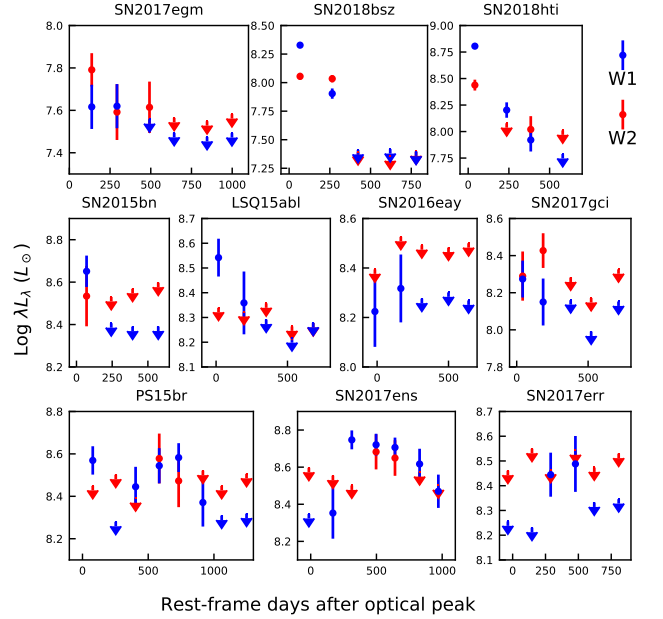


Figure 1. The MIR light curves of the 10 SLSNe with WISE detections. The luminosities at 3.4 and 4.6 μm are shown in blue and red, respectively.

they also have the same LC shape as the three closer SLSNe does not contradict the observations. Unlike them, PS15br’s MIR emission rebrightens at +404d after an initial decline between +78d and +253d. For SN 2017ens, although an initial decline was not recorded likely due to incomplete sampling, a late-time rebrightening can be clearly seen between +169d and +497d. SN 2017err’s W1-band fluxes on +289d and +477d show 2.3σ and 2.1σ increases compared with the flux on +147d. Combining the two, there is a 99.8% probability that a rebrightening is also seen in SN 2017err. The MIR rebrightening in the three SLSNe lasts at least one to two years. During the rebrightening, the MIR emission reach a peak monochromatic luminosity of $\sim 10^{8.5} L_\odot$ in both the two bands.

3.2 MIR Excess and Dust Properties

The early-time MIR emission in normal SNe can be the counterpart of the optical blackbody. While the late-time MIR emission, if present, usually exceeds the expected flux level inferred from optical data, and is likely the thermal emission of dust (e.g., Tinyanont et al. 2016; Szalai et al. 2019). The situation is likely similar in SLSNe. In this section, we are concerned with the MIR excess, i.e. the dust emission.

For SN 2015bn, LSQ15abl, and SN 2016eay, the MIR detections are at low levels possibly due to their greater distance ($z \sim 0.1$), and we did not analyse them in detail. We divided the remaining 7 SLSNe into two groups according to the presence of the rebrightening feature. We refer to the two groups as “declining group” and “rebrightening group” hereafter. The declining group includes SN 2017egm, SN 2017gci, SN 2018bsz, and SN 2018hti, and the rebrightening group includes PS15br, SN 2017ens, and SN 2017err.

3.2.1 The Declining Group

A red MIR color is a probe of dust emission among SNe. We show the variation of the WISE color $W1 - W2$ for the declining group in Fig. 2. The MIR colors of SN 2018bsz and SN 2018hti clearly turn red over time, and in the late time (after +200d or +300d) their colors ($W1 - W2 \sim 1.2$) correspond to blackbody temperatures (T_{BB}) of about 1000 K. The variation suggests that although their early-time MIR emission can be dominated by the long-wavelength tail of an optical/NIR blackbody, there must be significant dust emission in the late time. For example, assuming the spectrum is the sum of two blackbodies with T_{BB} of 6000 and 600 K, a color of $W1 - W2 \sim 1$ indicates that 70% of the $W2$ -band emission is from dust¹. For typical dust spectra, we calculated a conversion between $W1 - W2$ color and Spitzer/IRAC’s $I1 - I2$ color (see Appendix D for details) as:

$$I1 - I2 \approx 0.77(W1 - W2) - 0.02 \quad (1)$$

With this conversion, $W1 - W2 \sim 1.2$ corresponds to $I1 - I2 \sim 0.9$, consistent with those of normal SNe with dust emission detected (Szalai et al. 2021). We detected no significant changes in the MIR colors of SN 2017egm and SN 2017gci, and the red colors ($W1 - W2 \sim 1$) suggest that dust emission is also notable in them. Using data points with red colors ($W1 - W2 > 0.8$) and assuming that 50% \sim 100% of the $W2$ -band emission comes from dust, we estimated that the $W2$ -band monochromatic luminosity of the dust emission is $10^7 \sim 10^8 L_{\odot}$.

The dust emission in SN 2018bsz was well studied by Chen et al. (2022) combining with ground-based optical/NIR data as well as Spitzer MIR data. They concluded that the dust mass was between 10^{-4} and $10^{-2} M_{\odot}$. For the other three, although we cannot make a similar analysis due to a lack of data, we speculated that the dust mass is also between 10^{-4} and $10^{-2} M_{\odot}$ given that the three are similar to 2018bsz in MIR luminosity and color.

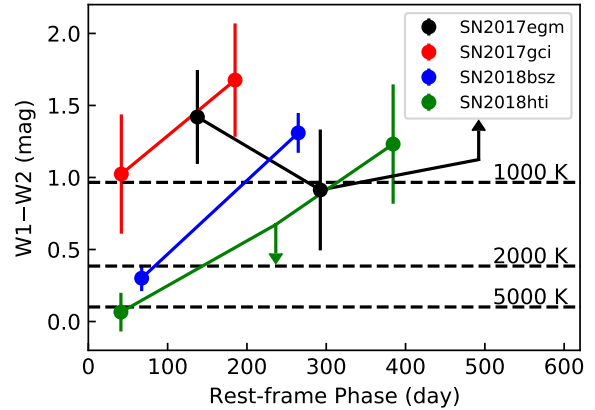


Figure 2. The variation of the MIR color $W1 - W2$ for the 4 SLSNe in the declining group. We show the MIR colors of blackbodies with T_{BB} of 1000, 2000, and 5000 K at $z = 0.05$ for a comparison.

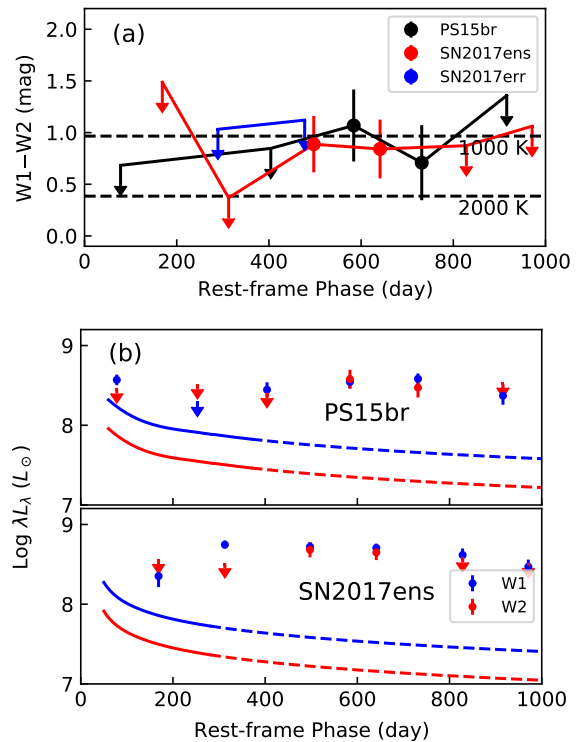


Figure 3. (a): The variation of the MIR color $W1 - W2$ for the 3 SLSNe in the rebrightening group. We show the MIR colors of blackbodies with T_{BB} of 1000 and 2000 K at $z = 0.1$ for a comparison. (b): The model LCs of the photosphere in $W1$ and $W2$ bands for PS15br and SN 2017ens, compared with the observed MIR data. We show the predictions by optical/NIR data with solid lines, and further extrapolations with dashed lines.

3.2.2 The Rebrightening Group

PS15br, SN 2017ens, and SN 2017err show rebrightenings with luminosities of $> 10^8 L_{\odot}$ 1 \sim 2 years after the optical

¹ $z = 0.05$ is assumed.

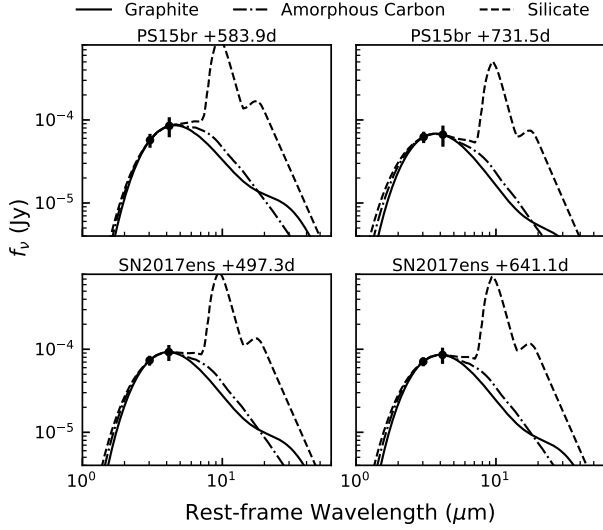


Figure 4. The SED fitting results for PS15br and SN 2017ens.

peak. A late-time MIR rebrightening among SNe is generally caused by delayed dust emission, and the same likely goes for the three SLSNe. As can be seen in Fig. 3(a), in the late time the MIR colors of the three SLSNe are $W1 - W2 \sim 1$, consistent with dust emission. We further estimated the contribution to the MIR emission by the SLSN photosphere in PS15br and SN 2017ens, which have abundant monitoring data in optical and NIR bands. We constructed the bolometric LCs for PS15br and SN 2017ens with methods described in detail in Appendix E. For both the two SLSNe, the temperature of the optical blackbody becomes stable to around 6000 K after +60d (Inserra et al. 2018; Chen et al. 2018). Thus we predicted the MIR flux of the SLSN photosphere by assuming a blackbody spectrum with a temperature of 6000 K. The results, displayed in Fig. 3(b), show that the SLSN photosphere contributes less than 15% to the W1-band flux, and less than 10% to the W2-band flux. Therefore the majority of MIR emission comes from dust during the rebrightening.

We measured the properties of the dust that causes the MIR rebrightening in PS15br and SN 2017ens using WISE observations showing detections in both the two bands. These include +584d and +732d observations for PS15br, and +497d and +641d observations for SN 2017ens. We fit the observed SED using models of dust emission. We assumed optically thin dust whose spectrum is expressed as (e.g., Hildebrand 1983; Fox et al. 2010):

$$L_\nu = 4\pi M_d B_\nu(T_d) \kappa_\nu(a), \quad (2)$$

where M_d is the dust mass, T_d is the dust temperature, B_ν is the Planck function, a is the grain radius, and κ_ν is the dust mass absorption coefficient. We tried dust compositions of graphite, amorphous carbon, and silicate², and adopted a grain radius of $0.1 \mu\text{m}$ following previous works (e.g., Tinyanont et al. 2016; Szalai et al. 2019). We show the models that match the observations in Fig. 4, and list the

² For graphite and silicate, we use the absorption coefficients from Fox et al. (2010). And for amorphous carbon, we use those from Rouleau & Martin (1991).

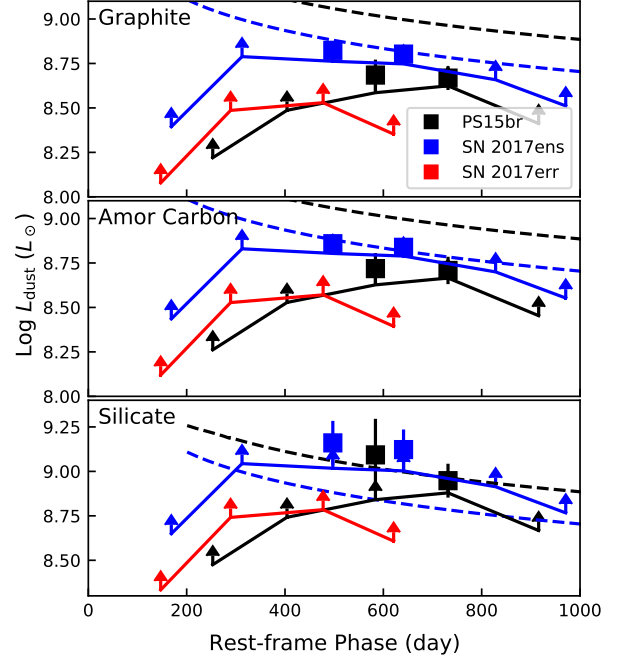


Figure 5. The L_{dust} curves for PS15br, SN 2017ens, and SN 2017err assuming different dust compositions. The squares are from spectral fitting, and the upper limits are converted from λL_λ in the W1 band. We also show the inferred bolometric LCs for PS15br and SN 2017ens for a comparison.

dust parameters in Tab. 2. We found that T_d are between 600 and 1100 K, and M_d are $(0.5 \sim 1.8) \times 10^{-2} M_\odot$ for graphite or amorphous carbon dust, and are $(1 \sim 4) \times 10^{-2} M_\odot$ for silicate dust. By integrating the best-fitting spectral model, we measured dust luminosities L_{dust} of $10^{8.6} \sim 10^{9.1} L_\odot$.

However, for most epochs of WISE observations, there is no significant detection in the W2 band, preventing us from calculating L_{dust} via a similar fitting. Nonetheless, there is a minimum integrated luminosity for SED models that are consistent with the only data point in the W1 band. This minimum value sets the lower limit of the L_{dust} . Considering bolometric correction C_B in the W1 band expressed as:

$$C_B = \frac{L_{\text{dust}}}{\lambda L_\lambda(W1)}. \quad (3)$$

For given dust properties and a given redshift, C_B is a function of the dust temperature T_d , as can be seen in detail in Appendix F. The function has a minimum value $\min(C_B)$ of 1.10, 1.21, and 1.98 for graphite, amorphous carbon, and silicate dust, respectively, at $z = 0.105$. Thus we obtain:

$$L_{\text{dust}} > \min(C_B) \times \lambda L_\lambda(W1). \quad (4)$$

In Fig. 5, we show the L_{dust} curves assuming different dust compositions. The dust luminosities are in the range of $10^8 \sim 10^9 L_\odot$.

We estimated the total energy of the dust emission as:

$$E_{\text{dust}} = \sum L_{\text{dust}} \times \Delta t, \quad (5)$$

where Δt is the time interval of WISE observations in the rest frame. The above summation includes all late-time WISE

Table 2. Dust parameters for PS15br and SN 2017ens

SLSN	Phase	Graphite		Amorphous Carbon		Silicate	
		t_d day	M_d $10^{-2}M_\odot$	t_d K	M_d $10^{-2}M_\odot$	t_d K	M_d $10^{-2}M_\odot$
PS15br	584	670 ± 120	$1.8^{+3.8}_{-1.2}$	780 ± 160	$1.6^{+3.5}_{-1.1}$	840 ± 190	$3.6^{+7.9}_{-3.0}$
	732	810 ± 170	$0.6^{+1.3}_{-0.4}$	990 ± 260	$0.5^{+1.1}_{-0.3}$	1080 ± 320	$1.1^{+2.6}_{-0.9}$
2017ens	497	740 ± 110	$1.4^{+2.0}_{-0.8}$	880 ± 160	$1.2^{+1.9}_{-0.7}$	950 ± 190	$2.8^{+4.2}_{-2.2}$
	641	760 ± 110	$1.2^{+1.7}_{-0.7}$	910 ± 170	$1.0^{+1.5}_{-0.6}$	980 ± 200	$2.3^{+3.5}_{-1.8}$

Table 3. Total Energy of Dust Emission

SLSN	E_{dust} (10^{50} erg)		
	Graphite	Amor Carbon	Silicate
PS15br	> 0.84	> 0.91	> 1.73
SN 2017ens	> 1.43	> 1.56	> 2.79
SN 2017err	> 0.48	> 0.53	> 0.87

observations as long as there are $> 2\sigma$ detections in the W1 band. For most epochs, there are only lower limits of L_{dust} , so we calculated the lower limit of E_{dust} . The results are listed in Tab. 3. For all the three SLSNe, the total energies are on the order of 10^{50} erg.

4 DUST ORIGIN AND HEATING MECHANISM

4.1 Time-delay Analysis

The MIR emitting dust around SNe can be pre-existing or newly formed. Pre-existing dust is sufficient to produce significant emissions only outside the dust-free cavity formed by the SNe. The radius of the dust-free cavity, known as evaporation radius r_{evap} , is determined by the SN peak luminosity L_{peak} (e.g., Dwek 1985; Fox et al. 2011) as:

$$r_{\text{evap}} = \left(\frac{L_{\text{peak}}}{16\pi\sigma T_{\text{evap}}^4 \langle Q \rangle (T_{\text{evap}})} \right)^{1/2}, \quad (6)$$

where σ is the Stefan-Boltzmann constant, T_{evap} is the vaporization temperature of the dust and $\langle Q \rangle (T_{\text{evap}})$ is the Planck-averaged value of the dust emissivity at the vaporization temperature. The emission from pre-existing dust is therefore delayed relative to the optical emission, and the time delay τ_{IR} , which is defined as the time relative to the optical peak, depends on the heating mechanism. If the dust is heated by the SN peak luminosity (IR echo), then $\tau_{\text{IR}} \sim r/c$, where r is the distance of the emitting dust, and c is the speed of light. Simulations (e.g., Dwek 1983, 1985) show that under typical conditions, the delay for 3–5 μm emission is about 1 ~ 10 times r_{evap}/c . If the dust is collisionally heated by shock, $\tau_{\text{IR}} \sim r/v_{\text{shock}} - t_{\text{rise}}$, where v_{shock} is the shock velocity, and t_{rise} is the time from the explosion to the optical peak. The shock velocity can be approximated by the photospheric velocity near the peak, which is between 6000 and 20,000 km s^{-1} for most SLSNe with a median value of 12,000 km s^{-1} , while the rise time of SLSNe is between 20 and 100 days with a median value of ~ 40 days (e.g., Quimby et al. 2018; Inserra et al. 2018; Könyves-Tóth & Vinkó 2021). There is also a time delay in the emission from newly formed dust because it takes time for the dust to form. For common core-collapse SNe (CCSNe), the MIR emission from newly formed dust becomes significant after several hundred days (e.g., Sugerman 2006; Szalai et al. 2021).

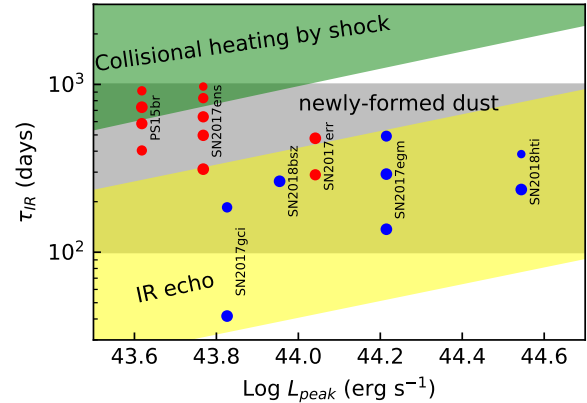


Figure 6. The τ_{IR} and L_{peak} for the seven SLSNe analysed in detail, and the constraint functions for dust models. The data for SLSNe in the dropping group and the rebrightening group are labeled using blue and red circles, respectively. The size of the circles represents the W1-band magnitude (larger for brighter), which is normalized using the peak value.

In Fig. 6, we display the τ_{IR} and L_{peak} ³ for the seven SLSNe with dust emission detected. We also show the constraint functions for different dust models for comparison. When calculating r_{evap} , one should note that the pre-existing dust may undergo twice radiative heating, one by the shock breakout and the other by the optical peak. Since the luminosity and duration of shock breakouts in SLSNe are loosely constrained, we estimated the lower limit of the r_{evap} by considering only the optical peak. We assumed graphite dust, and set grain size $a = 0.1 \mu\text{m}$ and $T_{\text{evap}} = 1900 \text{ K}$ following Dwek (1985). Under these assumptions, $r_{\text{evap}} = 0.11\sqrt{L_{44}}$ light-year, where L_{44} is the L_{peak} in unit of $10^{44} \text{ erg s}^{-1}$. For the IR echo case, we show the region with $r_{\text{evap}}/c < \tau_{\text{IR}} < 10r_{\text{evap}}/c$. For the shock-heating case, we show the region with $\tau_{\text{IR}} > r_{\text{evap}}/v_{\text{shock}} - t_{\text{rise}}$ by assuming a t_{rise} of 40 days and a v_{shock} of 12000 km s^{-1} . For the case of newly formed dust, we simply show a region between 100 and 1000 days. The τ_{IR} given by the shock-heating model is above 1000 days, and may be longer if considering the destruction of the pre-existing dust by the shock breakout. This is inconsistent with the observation, and therefore it is unlikely that the MIR emission of SLSNe comes from pre-existing dust heated by shock. It is difficult to draw conclusions on the IR echo and newly formed dust models simply based on time delay. We will discuss them in detail next.

³ The L_{peak} value of SN 2017err was calculated by us ($1.1 \times 10^{44} \text{ erg s}^{-1}$, see Appendix A), and those of the other SLSNe were collected from the literature.

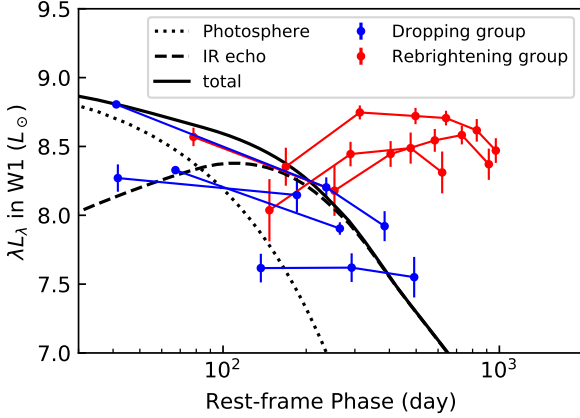


Figure 7. The data and simulated LC in the W1-band for the seven SLSNe analysed in detail.

4.2 IR Echo?

We simulated the IR echo of an SLSN and see what its MIR LC should look like. We ran the simulation following Dwek (1983, 1985) with the assumptions listed as followings. The SLSN has a peak luminosity $L_{\text{peak}} = 10^{44}$ erg s $^{-1}$ and drops exponentially after the peak with an e-folding time of $t_{\text{SN}} = 50$ day. The dust is distributed spherically symmetrically around the SLSN with an outer radius $R_2 = 3$ light-year. The dust is composed of graphite grains with a uniform radius of $a = 0.1$ μm . The peak SN luminosity causes a new spherical inner surface of dust with a radius $r_{\text{in}} = r_{\text{evap}} = 0.11$ light-year. The grain number density is inversely proportional to the square of the distance ($n_d \propto r^{-2}$), and the normalization is set so that the V-band attenuation A_V is 0.05. We display the W1-band LC from the simulation in Fig. 7. We found that the IR echo peaks with a time delay, which can be roughly expressed as $\tau_{\text{IR}} \sim 3r_{\text{evap}}/c$ when the dust is optically thin in the UV/optical bands, and is about 100 days for typical parameters. The peak W1-band luminosity is roughly proportional to n_d for a given grain radius, and is about $10^8 L_{\odot}$ under our assumptions. In addition, the model predicts that the MIR LC keeps decreasing after taking into account the photospheric emission.

For the four SLSNe in the dropping group, the observed MIR LC (blue points in Fig. 7) roughly agrees with the IR echo model in terms of time delay and luminosity. The inconsistency with the curve shown in Fig. 7 can be reconciled by adjusting the grain radius a and the number density n_d . The model predicts that the IR echo dominates the MIR emission after +100d, causing the MIR color to turn red. This is also consistent with the observations (see Fig. 2). Assuming that the echoing dust originates from the mass loss of the progenitor star, the n_d given by the model corresponds to a mass loss rate \dot{M} of $10^{-5} \sim 10^{-4} (f_d/0.01) (v_{\text{loss}}/100 \text{ km s}^{-1}) M_{\odot} \text{ yr}^{-1}$, where f_d is the mass fraction of the dust, and v_{loss} is the velocity of the mass loss. This rate is reasonable for high mass stars, which are possible SLSN progenitors. Thus the presence of echoing dust is natural.

However, for the three SLSNe in the rebrightening group, the above IR echo model can not reproduce the late time emission for two reasons. One reason is that the model predicts a peak before +200d while the observed LC peaks at

300–600 days. The second reason is that the predicted dust luminosity is not high enough when the dust is optically thin to the SLSN UV/optical emission ($A_V < 0.1$). Fitting the model to observations requires larger \dot{M} and larger r_{in} . Potential SN progenitors that have mass loss rate $\dot{M} > 10^{-4} M_{\odot} \text{ yr}^{-1}$ include luminous blue variable (LBV) stars (e.g. η Car, Smith et al. 2003), extreme red supergiant stars (e.g. VY CMa, Decin et al. 2006), and dusty Wolf-Rayet star (e.g. WR 48a, Zhekov et al. 2014). In addition, the dust around the LBV stars can be rich in silicate (e.g., Morris et al. 2017), which has a larger r_{evap} than graphite and may explain the large r_{in} required by the observations. Thus, using the IR echo model to explain the late-time MIR emission of the three SLSNe requires that the progenitor stars have extreme mass losses, and the dust is rich in silicates.

We tested the possibility by examining the energy balance and the required echoing dust. In section 3.2.2, we estimated the lower limit of the total energy of dust emission E_{dust} for the three SLSNe assuming silicate dust. The energies are at least $1.7\times$, $2.8\times$ and 0.9×10^{50} erg for PS15br, SN 2017ens and SN 2017err, respectively. However, the total energies released by PS15br and SN 2017ens near their peaks (<200 days after peak) are only about 3×10^{50} erg. Thus the IR echo model requires that almost all of the UV/optical emission near the peak is converted to IR emission by warm dust. In addition, the observed IR time delay requires that the warm dust is on the light-year scale. We show that these requirements can hardly be satisfied for the following three reasons. Firstly, the dust does not cover all directions because little dust extinction is observed in the light of sight, and hence some UV/optical emissions can escape. Secondly, part of scattered UV/optical emission and short-wavelength dust emission is absorbed with a large time delay, and the dust heated by them is likely too cold to generate significant $3 \mu\text{m}$ emission. Thirdly, assuming a typical grain radius distribution, for dust on a light-year scale to obscure optical emission, the required dust mass is at least $\sim 1 M_{\odot}$, which is too large even for η Car analogues. Therefore, IR echo cannot account for late-time MIR emission from PS15br and SN 2017ens. The peak luminosity of SN 2017err (1.1×10^{44} erg s $^{-1}$) is about twice those of PS15br and SN 2017ens (4.15 and 5.86×10^{43} erg s $^{-1}$, respectively). Assuming the bolometric LC of SN 2017err has the same shape as that of SN 2017ens, the near-peak UV/optical emission of SN 2017err is about 6×10^{50} erg, enough to power the observed dust emission with the energy of 1.2×10^{50} erg. Thus an IR echo model may apply to SN 2017err, although it is difficult to be fully tested due to insufficient data.

4.3 Echo of Shock Emission from CSM Interaction?

We found that the three SLSNe in the rebrightening group, including PS15br, SN 2017ens, and SN 2017err, all exhibit features of strong CSM interaction. PS15br shows a strong, multi-component H α emission after +200d, which was interpreted as an interaction of the ejecta with an asymmetric CSM (Inserra et al. 2018). In the late-time spectrum of SN 2017ens, Balmer emission lines consist of components with widths of ~ 2000 and several tens km s $^{-1}$, possibly representing postshock and undisturbed CSM, respectively (Chen et al. 2018). Also, strong coronal lines are present, possibly powered by the interaction. For SN 2017err, interaction is also

suggested by the narrow emission lines in the near-peak spectrum, which leads to an SLSN-II classification by Chen et al. (2017). These features of strong CSM interactions lead us to a conjecture: does the late-time MIR emission come from the pre-existing dust which is radiatively heated by shock emission, as supposed by Fox et al. (2010, 2011, 2013) for SN 2005ip and other SNe IIn?

We examined whether this model applies to PS15br and SN 2017ens. As can be seen from Fig. 5, the dust luminosity in the late time is close to the predicted power of shock emission. This requires thick asymmetric dust at a scale of several times r_{evap} (0.1–0.3 light-year), which absorbs most of the shock emission except for that escaping from the line of sight and converts it to IR emission. If such dust exists, it must also produce an IR echo in response to the peak SN luminosity. Based on the scale of the dust, we expected the echo to be observed within a few months after the optical peak. Assuming that most of the peak SN luminosity (with an energy of $\sim 3 \times 10^{50}$ erg) is absorbed and reradiated during these months, we estimated that the echo has an IR luminosity of several $10^9 L_{\odot}$. This hypothetical IR echo was not seen in the observations for PS15br on +78 day or SN 2017ens on +169 day. Thus it is unlikely that such thick dust exists. Therefore, we can rule out the shock emission heating model for PS15br and SN 2017ens. While for SN 2017err, as no luminous IR echo was seen in the observation on +147 day, this model is also unlikely to hold.

4.4 Newly Formed Dust?

Using detailed multi-band data and model analysis, Chen et al. (2022) demonstrated that the IR excess of SN 2018bsz can be explained by a newly formed dust model. SN 2017egm, SN 2017gci and SN 2018hti have similar LC and color evolution in the MIR band, so their IR excesses may also be explained by the same model. Here we focus on the three SLSNe showing rebrightening, especially PS15br and SN 2017ens with good data quality.

A newly formed dust model can generally explain some MIR rebrightenings in normal SNe (e.g. SN 2004dj, Szalai et al. 2011). We noted that the energy released from the cooling of newly formed dust from the condensation temperature is far from sufficient to power the observed IR luminosity of PS15br and SN 2017ens on the order of $> 10^8 L_{\odot}$ (see a similar argument for SN 2005ip in Fox et al. 2009), and there must be an additional heating source. As can be seen from Fig. 5, the dust luminosity is as high as $\sim 10^9 L_{\odot}$ even at about +600 days, and drops no more than 0.3 dex between +500 and +900 days, which corresponds to a drop rate of $< 0.2 \text{ mag } 100\text{d}^{-1}$. These can hardly be explained by heating by radiative decay of ^{56}Co or a magnetar which spins down. As we have seen features of strong CSM interaction in the two SLSNe, we inferred that the shock generated by the interaction can heat the dust. Such a model is described in detail in Smith et al. (2008) and Sarangi et al. (2018). Here we briefly introduced the model with an illustration in Fig. 8. The model assumes that dust forms in postshock clouds in a cool dense shell (CDS) located between the forward shock and the reverse shock. After being compressed by the shock, the cloud's temperature drops from $\sim 10^8$ K to $\sim 10^4$ K within a few days as it radiates most of its initial internal energy. The temperature then drops slowly because of addi-

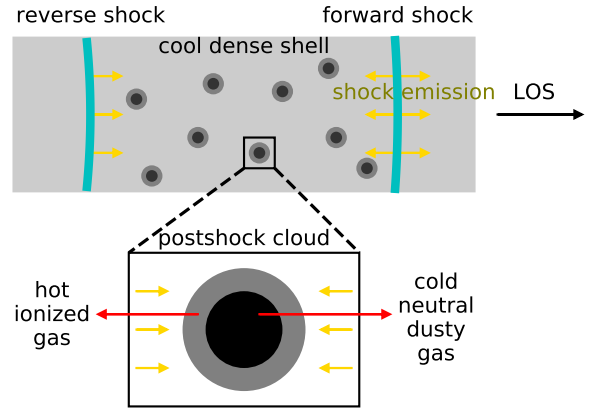


Figure 8. An illustration of the newly formed dust model for late-time MIR emission in some SNe with strong CSM interaction.

tional heating by shock emission, including inward emission from the forward shock, and the outward emission from the reverse shock. As the shock emission weakens and the CDS scales up in a few hundred days, the temperature in the core of the cloud drops to the condensation temperature, and dust begins to form. The newly formed dust is heated by shock emission in two ways. On one hand, the UV/optical emission is directly absorbed by the dust. On the other hand, the far-UV and soft X-ray emission heats the ambient gas, and indirectly heats the dust via reradiation from the gas or collision by the gas. The heated newly formed dust explains the observed IR emission at the late time. To check whether such a model is suitable for the two SLSNe, we made the following four tests.

The first test is that the dust is located in a spherical shell behind the forward shock. That is, $r_{\text{dust}} < r_{\text{FS}}$, where r_{dust} is the outer radius of this shell and r_{FS} is the radius of the forward shock. We estimated the r_{dust} in PS15br and SN 2017ens using blackbody radius r_{bb} obtained by fitting the SED with blackbody curves, which is shown in Fig. 9(a). As can be seen in Fig. 9(a), $r_{\text{bb}} < r_{\text{FS}}$ requires a shock velocity of at least $\sim 10000 \text{ km s}^{-1}$ assuming homogeneous expansions. Such values are possible as SLSNe typically show higher shock velocities than normal SNe (Inserra et al. 2018; Könyves-Tóth & Vinkó 2021).

The second test is about energy balance: the observed dust luminosity cannot exceed the heating power at a certain time. In Fig. 5, we compare the observed L_{dust} curves and the predicted radiant power of the shock (L_{shock}) for PS15br and SN 2017ens (see Appendix E for the details of the model, note that L_{bol} is dominated by L_{shock} after 200 days). We found that after around +500d, the MIR LC declines in step with L_{shock} . This is evidence that the dust luminosity is limited by the heating power. Assuming amorphous carbon or silicate dust, the dust luminosity is roughly consistent with the predicted L_{shock} considering the uncertainties in the models.

The third test is that the postshock clouds can be cool enough for the dust to form. Using abundant multi-band data, Sarangi et al. (2018) estimated how L_{shock} and the scale of CDS vary with time in SN 2010jl, and inferred that dust can form 380 days after the explosion. We assumed that the dust can also form in the two SLSNe when the similar $L_{\text{shock}}/r_{\text{FS}}^2$ values are obtained. The estimated L_{shock} of $\sim 10^9$

L_{\odot} in PS15br and SN 2017ens at around +400 days is similar to that in SN 2010jl at similar epochs. If assuming r_{FS} close to that of SN 2010jl at similar epochs, the dust can form in the two SLSNe at around 400 days. Moreover, if assuming a larger r_{FS} , as suggested by larger r_{BB} at around +600 days ($\sim 6 \times 10^{16}$ cm for PS15br and SN 2017ens and $\sim 3 \times 10^{16}$ cm for SN 2010jl), the dust can form earlier. The predicted onset of dust formation, +300 \sim +400 days, is consistent with the observed time of MIR rebrightening.

The final test is about the required dust mass. In Fig. 9(b) we show the dust mass M_d in PS15br and SN 2017ens, which was obtained in Section 3.2.2 from SED fitting by assuming optically thin dust with grain radius of 0.1 μm . One should treat these values with caution because measurements of M_d in SNe are usually model-dependent. We examined the uncertainty that may arise from different model assumptions. The optical depth at $\sim 4 \mu\text{m}$ of a homogeneous dust sphere with a radius r can be expressed as:

$$\tau(\lambda) = \frac{3\kappa(\lambda)M_d}{4\pi r^2} = \tau_0 \left(\frac{M_d}{10^{-2} M_{\odot}} \right) \left(\frac{r}{10^{17} \text{ cm}} \right)^{-2} \quad (7)$$

where τ_0 is 0.4 and 0.13 for amorphous carbon and silicate dust, respectively. Using the measured M_d for PS15br and SN 2017ens and assuming $r = r_{\text{bb}} \sim 10^{16.8}$ cm, the optical depth is about 1, and hence the optically thin assumption that we used may hold. However, optically thick dust is possible. If so, the M_d estimated earlier is only the mass in the $\tau < 1$ layer, and the total M_d needs to be multiplied by the IR optical depth. In addition, if different grain radii are assumed, the resulting M_d is also different. Following some previous works (e.g., Stritzinger et al. 2012), we re-measured the M_d assuming grain radii of 0.01 and 1 μm , and found several times differences. In summary, our M_d measurements can be conservative order-of-magnitude estimations. We also show the measurements of M_d for SN 1987A (Wesson et al. 2015), SN 2010jl (Gall et al. 2014) and SN 2018bsz (Chen et al. 2022) in Fig. 9(b) for a comparison. The M_d in PS15br and SN 2017ens at around +600d are about one order of magnitude higher than the values of SN 1987A and SN 2010jl at similar epochs, and nevertheless is within the scope of dust formation theory (e.g., Sarangi 2018). In particular, the M_d are consistent with that of SN 2018bsz in similar phases, which is predicted by the evolutionary trend assuming that $M_d \propto t^{2.4}$ (Chen et al. 2022).

The newly formed dust model passes the tests described above. Therefore we conclude that the late-time MIR emission of PS15br and SN2017ens can be explained by newly formed dust. For SN2017err, although there is not enough data for the above tests, the late-time MIR emission may also be explained by the same model, because its MIR LC is similar to those of PS15br and SN 2017ens.

4.5 A Summary on Dust Origin and Heating Mechanism

In SN 2017egm, SN 2017gci, SN 2018bsz and SN 2018hti, dust emission appears between +100d and +500d with a monochromatic luminosity of $10^7 \sim 10^8 L_{\odot}$. In terms of time delay and luminosity, the dust emission can be explained by both the IR echo model and the newly formed dust model. Distinguishing the two models may rely on multi-band monitoring data and detailed model analysis. An example was

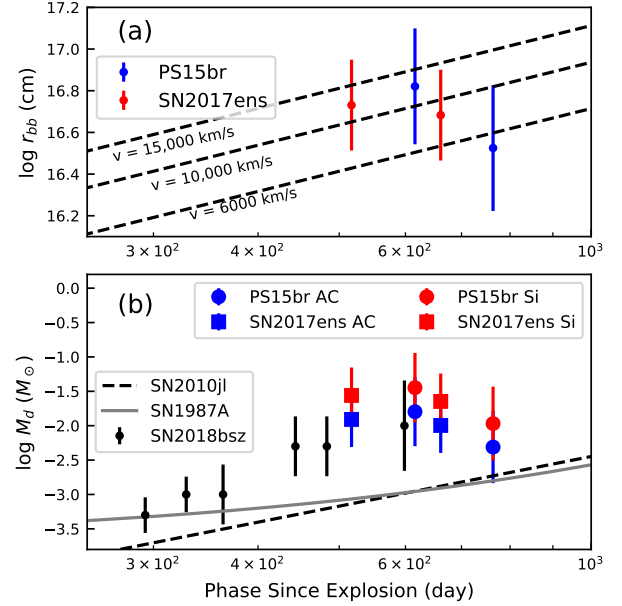


Figure 9. (a): The r_{bb} during the rebrightening in PS15br and SN 2017ens, and the shock expanding model that fit the data. In this plot, the phases are all relative to the explosion date. (b): The dust masses inferred for PS15br and SN 2017ens. We show the evolutions of M_d of SN 1987A, SN 2010jl, and SN 2018bsz for a comparison.

presented in Chen et al. (2022) for SN2018bsz. Chen et al. demonstrated that an IR echo model can hardly explain the dust emission. The strongest evidence is that the optical monitoring did not detect scattered optical emission in step with the dust IR emission, which is predicted by the echo model. Similar analysis can be made for other SLSNe to figure out the dust origin in the future.

In PS15br and SN2017ens, dust emission appears up to around +1000d with a luminosity of $10^8 \sim 10^9 L_{\odot}$. The late-time emission can hardly be explained as an IR echo of the peak luminosity or an echo of the late-time shock emission, while can be naturally explained as the emission from newly formed dust. Based on SED fittings, we estimated that dust with a mass of $\sim 10^{-2} M_{\odot}$ has been formed around 600 days after the explosion. For SN 2017err, we failed to distinguish between IR echo and newly formed dust models because of insufficient data. Anyhow, assuming that its late-time MIR emission comes from newly formed dust, a unified picture of the three SLSNe showing rebrightening features can be drawn.

5 DISCUSSIONS

5.1 The Cause of The MIR Rebrightening

What causes the MIR rebrightening by several hundred days in 3 out of 11 SLSNe? We first check if this is related to the spectral types of the SLSNe, which were classified according to the near-peak spectra. The three SLSNe, PS15br, SN 2017ens, and SN 2017err belong to type II, type I, and type II_n, respectively. This implies that SLSNe of various spectral types may show MIR rebrightening. The situation is similar

to normal SNe: SNe with MIR rebrightening belongs to various spectral types such as Ia-CSM, Ib, IIP, and IIn (e.g., [Tinyanont et al. 2016](#); [Szalai et al. 2019](#)). So it is likely that the spectral type is not the determining factor for showing MIR rebrightening.

As we have pointed out in Section 4.3, all of the three SLSNe in the rebrightening group show features of strong interaction in their spectra. A correlation between CSM interaction and late-time MIR rebrightening is also present in normal SNe. For example, Ia-CSM and IIn are types of SNe that most frequently exhibit MIR rebrightening (e.g., [Fox et al. 2013](#); [Szalai et al. 2019](#)). Therefore it is likely that the MIR rebrightening in the three SLSNe is related to the CSM interaction.

The bolometric LCs of PS15br and SN 2017ens drop more slowly than other SLSNe in the late time ([Inserra et al. 2018](#); [Chen et al. 2018](#)). The best explanation for their slowly declining LCs is the radiant energy from shock, which is released during the CSM interaction. Regardless of the energy source in the early time, the heating by interaction becomes dominant after about one year at the latest. The emission from the reverse shock and the inward emission from the forward shock can be absorbed by the newly formed dust. As the dust accumulates, an increasing proportion of the energy is transferred from the optical or X-ray bands to the IR band. This explains the rise in the MIR LC. When the amount of dust increases enough to convert most of the energy, the dust luminosity decreases slowly due to the limitation of the heating power. This is consistent with the observation, as can be seen in Fig. 5. This scenario can be tested by future observations with better data quality in the JWST era.

The situation is different for those SLSNe without strong interaction, such as SN2018bsz ([Chen et al. 2022](#)). The newly formed dust, if present, can only be heated by radiative decay of ^{56}Co or by magnetar. The heating power drops off rapidly, and hence the emission from the newly formed dust is not strong enough to produce an observed rebrightening feature in the MIR LC.

5.2 SLSNe as More Productive Dust Factories?

[Chen et al. \(2022\)](#) demonstrated that SN 2018bsz possibly forms ten times more dust than normal CCSNe at similar epochs. They further suggested that SLSNe may contribute $\sim 10\%$ of dust formation in the early universe with the following assumptions. Firstly, all the SLSNe have high dust formation efficiencies. Secondly, the final dust mass is also ten times different. Thirdly, the proportion of SLSNe in CC-SNe is 1% in the early universe. We found evidence that the dust mass in PS15br and SN2017ens is also ten times higher than normal CCSNe at the same epoch. Our results appear to support the first hypothesis of [Chen et al. \(2022\)](#).

However, more observations are required to conclude that SLSNe are more productive dust factories. If the dust forms rapidly and is optically thick in a few years, as suggested by [Dwek et al. \(2019\)](#), then the higher dust mass observed in SLSNe may simply be because the ejecta expands faster, causing more dust to be exposed. Assuming that the newly formed dust in PS15br and SN2017ens is inside an expanding sphere, the required expansion velocity is as high as ~ 10000 km s $^{-1}$, much higher than the typical value (2000–3000 km s $^{-1}$ for the inner ejecta) in normal CCSNe (e.g., [Szalai &](#)

[Vinko 2013](#)). A 3-fold difference in the ejecta velocity, and a corresponding 10-fold difference in the surface area of the dust sphere, is sufficient to explain the difference in the observed dust mass without additional assumptions about different dust formation efficiencies. In addition, there is a possibility that the final dust mass is not greater in SLSNe though dust forms more rapidly in the first few years. To check these possibilities and draw final conclusions on the dust formation efficiency in SLSNe require longer monitorings up to decades in the future.

5.3 Is There an Upper Limit to The MIR Luminosity of SNe?

[Szalai et al. \(2019\)](#) collated the Spitzer observations of 693 SNe with known redshift. They found that the most MIR luminous SNe are of the IIn and Ia-CSM types, although these are only a small proportion of the total SNe. Among the sample of Szalai et al., the SNe with the highest MIR luminosity is SN 2010jl and SN 2013cj, both of which are of the IIn type. The absolute magnitudes of these two SNe are around -22.2 at $3.6 \mu\text{m}$ and around -22.8 at $4.5 \mu\text{m}$. [Jiang et al. \(2019\)](#) examined the WISE data of some known SNe with small angular separations from the galaxy centers. They supplemented two normal SNe with luminosities similar to SN 2010jl, including SN 2013dz⁴ and SN 2014ab (also reported in [Moriya et al. 2020](#)), which are also of the IIn type. Interestingly, they found that ASASSN-15lh is extremely luminous in the MIR with W2-band absolute magnitude around -25 , which is >2 magnitudes more luminous than the above-mentioned SNe IIn. Note that the nature of ASASSN-15lh is unclear. The discovery work ([Dong et al. 2016](#)) considered it to be an SLSN, while some follow-up works (e.g., [Krühler et al. 2018](#)) considered it to be a TDE.

In the last decade, there have been a number of transient events occurring at the centers of galaxies that are difficult to categorize unambiguously. These events include CSS100217:102913+404220 ([Drake et al. 2011](#); [Zhang et al. 2022](#)), PS16dtm ([Blanchard et al. 2017](#); [Jiang et al. 2017](#)), a flare in WISEA J094806.56+031801.7 ([Assef et al. 2018](#)), in addition to ASASSN-15lh. All of these events have strong MIR emissions with peak W2-band absolute magnitudes between -25 and -28 . This makes an SNe identification controversial, as normal SNe is not so bright in the MIR band. Moreover, IR flares with a week or no optical counterpart in the centers of some galaxies have recently been reported. Examples are Arp-299B AT1 ([Mattila et al. 2018](#)), SDSS J165726.81+234528.1 ([Yang et al. 2019](#)), MCG-02-04-026 ([Sun et al. 2020](#)), AT 2017bgl ([Kool et al. 2020](#)) and a sample of several tens MIR flares reported by [Jiang et al. \(2021\)](#). They were generally considered to be dust-obscured transient events, which may be TDE, SNe, or active galactic nuclei flares. Although the nature of a few flares can be inferred from radio observations (e.g., [Mattila et al. 2018](#)), most flares have only IR information available.

The above situation leads one to an idea: is it possible to conclude that a flare is not an SN on the ground of too high MIR luminosity? However, some previous works failed

⁴ Note that [Jiang et al. \(2019\)](#) misspelled it as SN2013dy

to fully address this issue due to the lack of a comprehensive understanding of the MIR emission of SLSNe.

The SLSNe in our sample have peak W2-band absolute magnitudes between -21.5 and -23 . They are not more MIR luminous than the most luminous SN IIn, though they are indeed more luminous than normal SNe on average. Our results seem to support an upper limit on the MIR luminosity of SNe, though the sample size of 11 is not large.

A possible explanation is as follows. MIR emission from SNe comes from IR echo or dust heated locally in the late time. On one hand, the luminosity of the IR echo depends on the optical depth of the CSM dust to the SN UV/optical emission. Echoing dust must be located outside the evaporation radius, which is expected to be between 0.1 and 1 light-year for the brightest SNe. In addition, only echo from dust within a couple of light-years can emit significantly in the 3–5 μm band, and more distant dust produces an echo with lower luminosity or with SED peaks at longer wavelengths. To make CSM dust thick enough to obscure the UV/optical emission, the required mass loss rate $\sim 10^{-1}(f_d/0.01)(v_{\text{loss}}/100 \text{ km s}^{-1}) M_{\odot} \text{ yr}^{-1}$ can hardly be satisfied even by LBV stars. Assuming that CSM dust absorbs 1% to 10% of the SNe UV/optical emission and that the duration of the IR echo is 10 times longer, a peak bolometric luminosity of $10^{11} L_{\odot}$ only results in a dust luminosity of 10^8 – $10^9 L_{\odot}$. On the other hand, the luminosity from locally heated dust is limited by both the size of the dust sphere and the heating power. In the earlier time, L_{dust} does not exceed $4\pi v_{\text{shock}}^2 t^2 \sigma T_d^4$. And when the dust sphere is large enough with the expansion of the shock, typically after a few hundred days, the heating power decreases because the central magnetar spins down or the density of interacting CSM decreases. Therefore, there is an upper limit on the MIR luminosity of the emission produced by both mechanisms.

6 CONCLUSIONS

We have presented and analysed the MIR properties at 3.4 and 4.6 μm from a sample of 11 SLSNe, and investigated the dust emission in 7 of them. The results are as follows.

1. MIR emission is detected from 10 out of 11 SLSNe with a threshold corresponding to luminosities at 3.4 and 4.6 μm of $\sim 10^8 L_{\odot}$. Most of the SLSNe show declining LCs and fade in about one year after the optical peak. While the LCs of 3 SLSNe show a rebrightening in 1–2 years, and finally fade in 2–3 years.

2. Dust emission is detected in 7 SLSNe according to the MIR color of $W1 - W2 \sim 1$ or the rebrightening feature in the LC. For further study, we divided these 7 into two groups, a declining group including SN 2017egm, SN 2017gci, SN 2018bsz, and SN 2018hti, and a rebrightening group including PS15br, SN 2017ens, and SN 2017err. For the declining group, the dust emission was detected about 100–500 days after the optical peak. The dust emits in the MIR band with a monochromatic luminosity of $10^7 \sim 10^8 L_{\odot}$. The dust masses may be 10^{-4} – $10^{-2} M_{\odot}$. For the rebrightening group, the dust emission can be detected about 400–1000 days after the optical peak. The dust luminosities are $10^8 \sim 10^9 L_{\odot}$ and the total energies of dust emission are $\sim 10^{50}$ erg. The dust has a temperature of 600–1100 K, and its mass is $\sim 1 \times 10^{-2}$

or $\sim 3 \times 10^{-2} M_{\odot}$ if assuming carbonaceous or silicate dust, respectively, with grain radii of 0.1 μm .

3. For the declining group, the dust emission can be explained using both an IR echo model and a newly formed dust model. While for PS15br and SN 2017ens, the late-time (after ~ 1 years) MIR emission can only be explained by a newly formed dust model. In this model, dust with a mass of $\gtrsim 10^{-2} M_{\odot}$ has formed ~ 600 days after the explosion.

4. Considering that all the three SLSNe in the rebrightening group show features of strong CSM interaction, we conclude that newly formed dust heated by interaction explains the late-time dust emission with $10^8 \sim 10^9 L_{\odot}$ and the rebrightenings in the LCs. The absence of strong late-time dust emission in other SLSNe may be due to the lack of interaction to provide enough heating power.

5. Taking into account our measurements of dust formations for PS15br and SN 2017ens and the measurement for SN 2018bsz by Chen et al. (2022), it seems that SLSNe form one order-of-magnitude more dust than normal SNe in the same phase. However, to draw conclusions about whether SLSNe have higher dust formation efficiency, decades of monitoring are necessary.

6. We found that the MIR luminosity of SLSNe is on average higher than normal SNe. However, except for ASASSN-15lh whose SLSN nature is under debate, SLSNe are not more MIR luminous than SNe IIn. Thus MIR flares more luminous than SLSNe and SNe IIn are more likely to be associated with TDE or active galactic nuclei flares rather than SNe.

ACKNOWLEDGEMENTS

We thank the anonymous referee for helping us improve the work. We thank T. Chen, C. Inserra, and S. Smartt for providing us SLSNe data. L. Sun acknowledges the support from National Natural Science Foundation of China (NFSC, grant No. 12103002), and from Anhui Provincial Natural Science Foundation (grant No. 2108085QA43). L. Xiao is thankful for the support from NFSC (grant No. 12103050), Advanced Talents Incubation Program of the Hebei University, and Midwest Universities Comprehensive Strength Promotion project. This publication makes use of data products from the Wide-field Infrared Survey Explorer, which is a joint project of the University of California, Los Angeles, and the Jet Propulsion Laboratory/California Institute of Technology, funded by the National Aeronautics and Space Administration.

DATA AVAILABILITY

Any new data used in this paper is available in the Appendix.

REFERENCES

- Alard, C., Lupton, Robert H., 1998, ApJ, 503, 325
- Alard, C., 2000, A%AS, 144, 363
- Anderson, J. P., Pessi, P. J., Dessart, L., et al., 2018, A%A, 620, 67
- Assef, R. J., Prieto, J. L., Stern, D., Cutri, R. M., et al., 2018, ApJ, 866, 26

- Baltay, Charles, Rabinowitz, David, Hadjijska, Elena, et al., 2013, *PASP*, 125, 683
- Bertin, Emmanuel, 2010, *Astrophysics Source Code Library*, 1010.068
- Bhimbhakkadi, Kornpob, Chornock, Ryan, Miller, Adam A., et al., 2019, *MNRAS*, 488, 3783
- Blanchard, P. K., Nicholl, M., Berger, E., Guillochon, J., et al., 2017, *ApJ*, 843, 106
- Bose, S., Dong, Subo, Pastorello, A., et al., 2018, *ApJ*, 853, 57
- Brown, P. J., Breeveld, A. A., Holland, S., et al., 2014, *ApJ*, 785, 89
- Chen, T.-W., Wyrzykowski, L., Gromadzki, M., et al., 2017, *The Astronomer's Telegram*, 10535
- Chen, T.-W., Inerra, C., Fraser, M., et al., 2018, *ApJ*, 867, 31
- Chen, T.-W., Brennan, S. J., Wesson, R., 2022, arXiv:2109.07942
- Decin, L., Hony, S., de Koter, A., et al., 2006, *A&A*, 456, 549
- Dong, S.-B., Shappee, B. J., Prieto, J. L., Jha, S. W., et al., 2016, *Sci*, 351, 257
- Drake, A. J., Djorgovski, S. G., Mahabal, A., Anderson, J., et al., 2011, *ApJ*, 735, 106
- Dwek, E., 1983, *ApJ*, 274, 175
- Dwek, E., 1985, *ApJ*, 297, 719
- Dwek, E., Sarangi, A., Arendt, R. G., 2019, *ApJ*, 871, 33
- Fiore, A., Chen, T.-W., Jerkstrand, A., et al., 2021, *MNRAS*, 502, 2120
- Fox, Ori D., Skrutskie, Michael F., Chevalier, Roger A., et al., 2009, *ApJ*, 691, 650
- Fox, Ori D., Chevalier, Roger A., Dwek, E., et al., 2010, *ApJ*, 725, 1768
- Fox, Ori D., Chevalier, Roger A., Skrutskie, Michael F., et al., 2011, *ApJ*, 741, 7
- Fox, Ori D., Filippenko, Alexei V., Skrutskie, Michael F., et al., 2013, *AJ*, 146, 2
- Fox, Ori D., Smith, Nathan, Ammons, S. Mark, et al., 2015, *MNRAS*, 454, 4366
- Gal-Yam, A., Mazzali, P., Ofek, E. O., et al., 2009, *Natur*, 462, 624
- Gal-Yam, Avishay, 2012, *Science*, 337, 927
- Gal-Yam, Avishay, 2019, *ARA&A*, 57, 305
- Gall, Christa, Hjorth, Jens, Watson, Darach, et al., 2014, *Natur*, 511, 326
- Guillochon, James, Parrent, Jerod, Kelley, Luke Zoltan, et al., 2017, *ApJ*, 835, 64
- Hildebrand, R. H., 1983, *QJRAS*, 24, 267
- Inerra, C., Smartt, S. J., Gall, E. E. E., et al., 2018, *MNRAS*, 475, 1046
- Jiang, N., Wang, T.-G., Yan, L., et al., 2017, *ApJ*, 850, 63
- Jiang, N., Wang, T.-G., Mou, G.-B., Liu, H., et al., 2019, *ApJ*, 871, 15
- Jiang, N., Wang, T.-G., Dou, L.-M., et al., 2021, *ApJS*, 252, 32
- Kokubo, M., Mitsuda, K., Morokuma, T., et al., 2019, *ApJ*, 872, 135
- Könyves-Tóth R., Vinkó, J., 2021, *ApJ*, 909, 24
- Kool, E. C., Reynolds, T. M., Mattila, S., et al., 2020, *MNRAS*, 498, 2167
- Krühler, T., Fraser, M., Leloudas, G., Schulze, S., et al., 2018, *A&A*, 610, 14
- Lang, D., Hogg, D. W., Schlegel, D. J., 2016, *AJ*, 151, 36
- Lin, W. L., Wang, X. F., Li, W. X., et al., 2020, *MNRAS*, 497, 318
- Lunnan, R., Yan, Lin, Perley, D. A. et al. 2020, *ApJ*, 901, 61
- Mainzer, A., Grav, T., Bauer, J., et al., 2011, *ApJ*, 743, 156
- Mainzer, A., Bauer, J., Cutri, R. M., et al., 2014, *ApJ*, 792, 30
- Meisner, A. M., Lang, D., Schlegel, D. J., 2018, *AJ*, 156, 69
- Mattila, S., Pérez-Torres, M., Efstathiou, A., et al., 2018, *Sci*, 361, 482
- Miller, A. A., Smith, N., Li, W., et al., 2010, *AJ*, 139, 2218
- Moriya, T. J., Stritzinger, M. D., Taddia, F., 2020, *A&A*, 641, 148
- Morris, Patrick W., Gull, Theodore R., Hillier, D. John, 2017, *ApJ*, 842, 79
- Nicholl, M., Berger, E., Smartt, S. J., et al., 2016, *ApJ*, 826, 39
- Nicholl, M., Berger, E., Margutti, R., et al., 2017, *ApJ*, 835, 8
- Perley, D. A., Quimby, R. M., Yan, L., et al., 2016, *ApJ*, 830, 13
- Planck Collaboration et al. 2016, *A&A*, 594, 13
- Prajs, S., Cartier, R., Frohmaier, C., et al., 2015, *The Astronomer's Telegram*, 7412
- Prieto, J. L., Lee, J. C., Drake, A. J., et al., 2012, *ApJ*, 745, 70
- Quimby, R. M., Kulkarni, S. R., Kasliwal, M. M., et al., 2011, *Natur*, 474, 487
- Quimby, R. M., De Cia, A., Gal-Yam, A., et al. 2018, *ApJ*, 855, 2
- Rouleau, Francois, Martin, P. G. 1991, *ApJ*, 377, 526
- Sarangi, A., Matsuura, M., Micelotta, E. R., 2018, *SSRv*, 214, 63
- Sarangi, Arkaprabha, Dwek, Eli, Arendt, Richard G., 2018, *ApJ*, 859, 66
- Sugerman, Ben E. K., Ercolano, Barbara, Barlow, M. J., 2006, *Sci*, 313, 196
- Smith, Nathan, Gehrz, Robert D., Hinz, Philip M., et al., 2003, *AJ*, 125, 1458
- Smith, Nathan, Li, Weidong, Foley, Ryan J., et al., 2007, *ApJ*, 666, 1116
- Smith, Nathan, Foley, Ryan J., Filippenko, A. V., et al., 2008, *ApJ*, 680, 568
- Smith, Nathan, Foley, Ryan J., Bloom, Joshua S., et al., 2008, *ApJ*, 686, 485
- Smith, Nathan, Silverman, Jeffrey M., Chornock, Ryan, et al., 2009, *ApJ*, 695, 1334
- Smith, K. W., Smartt, S. J., Young, D. R., et al., 2020, *PASP*, 132, 085002
- Sukhbold, Tuguldur, Woosley, S. E., 2016, *ApJ*, 820, 38
- Stritzinger, Maximilian, Taddia, Francesco, et al., 2012, *ApJ*, 756, 173
- Sun, Luming, Jiang, Ning, Wang, Tinggui, et al., 2020, *ApJ*, 898, 129
- Szalai, T., Vinko, J., Balog, Z., et al. 2011, *A&A*, 527, 61
- Szalai, T., Vinko, J., 2013, *A&A*, 549, 79
- Szalai, Tamas, Zsiros, Szanna, Fox, Ori D., et al., 2019, *ApJS*, 241, 38
- Szalai, Tamas, Fox, Ori D., Arendt, Richard G., et al., 2021, *ApJ*, 919, 17
- Tartaglia, L., Pastorello, A., Sollerman, J., 2020, *A&A*, 635, 39
- Tinyanont, Samaporn, Kasliwal, Mansi M., Fox, Ori D., et al., 2016, *ApJ*, 833, 231
- Tonry, J. L., 2011, *PASP*, 123, 58
- Tonry, J. L., Denneau, L., Heinze, A. N., *PASP*, 130, 064505
- Wesson, R., Barlow, M. J., Matsuura, M., et al. 2015, *MNRAS*, 446, 2089
- Wright, E. L., Eisenhardt, P. R. M., Mainzer, A. K., et al., 2010, *AJ*, 140, 1868
- Yan, Lin, Quimby, R., Gal-Yam, A. et al., 2017, *ApJ*, 840, 57
- Yang, Qian, Shen, Yue, Liu, Xin, Wu, Xue-Bing, et al., 2019, *ApJ*, 885, 110
- Yaron, Ofer, Gal-Yam, Avishay, 2012, *PASP*, 124, 668
- Zhang, W.-J., Shu, X.-W., Sheng, Z.-Y., 2022, *A&A*, accepted
- Zhekov, S. A., Tomov, T., Gawronski, M. P., et al., 2014, *MNRAS*, 445, 1663

APPENDIX A: THE OPTICAL DATA OF LSQ15ABL AND SN 2017ERR

LSQ15abl was discovered on 2015 Mar 19 by La Silla-Quest survey (LSQ, Baltay et al. 2013). Prajs et al. (2015) identified it as SLSN-II, and measured a redshift of 0.087. The SNe was monitored by Swift/UVOT between 2015 Apr 21 and 2015 Oct 10 in all six bands. We show the V-band LC in Fig. A, using the LSQ magnitude reported in Prajs et al. and the Swift/UVOT magnitudes from Swift's Optical/Ultraviolet

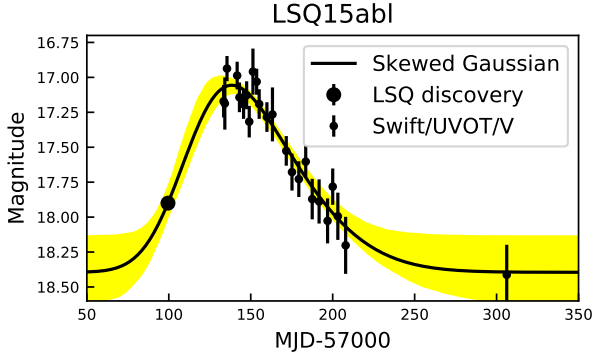


Figure A1. : The V-band LC of LSQ15abl and the skewed Gaussian model fitting to it.

Supernova Archive (SOUSA Brown et al. 2014). The LC can be fitted using a skewed Gaussian curve, and with the curve, we measured a peak of the LC at MJD= 57136 \pm 5 (2015 Apr 24).

SN 2017err was discovered on 2017 Jun 12 with o-band magnitude of 18.3 \pm 0.1 (Chen et al. 2017) by Asteroid Terrestrial-Impact Last Alert System (ATLAS, Tonry 2011). From the ATLAS team (S. Smartt, private communication), SN2017err continued to rise to a measured brightest magnitude of $m = 17.7 \pm 0.1$ on MJD= 57939. The ATLAS flux measurements and calibration are carried out on the difference images as described in Tonry et al. (2018) and Smith et al. (2020). Although given the faint magnitude of the host of $r = 20.3$, there was little contamination at the peak. After a gap in observing this position, ATLAS detected this object fading on MJD= 58054 at $m = 18.8 \pm 0.2$. The ATLAS team reports that the gap in observing makes a true peak estimate uncertain, but it papers to be MJD= 57935 \pm 10 days. According to the optical/NIR follow-up observation taken on MJD= 57924 ($g' = 17.92 \pm 0.07$, $r' = 18.01 \pm 0.10$, $i' = 18.07 \pm 0.07$, $z' = 18.24 \pm 0.07$, $J = 18.96 \pm 0.13$, and $H = 19.14 \pm 0.19$, all in the AB system), we measured a blackbody temperature of SN 2017err of 12400 \pm 900 K. Using this temperature, the peak magnitude was converted to a bolometric luminosity of 1.1×10^{44} erg s $^{-1}$.

APPENDIX B: THE IMAGE SUBTRACTION RESULTS

The reference, target, and difference images are shown in Fig. B. The photometries are listed in Tab. B1.

APPENDIX C: A CHECK OF WISE PHOTOMETRY OF SN 2018BSZ WITH SPITZER RESULT

SN 2018bsz is the only SLSNe in our sample which was observed by Spitzer. IRAC observations were taken on +384, +403, +535 and +564 days with I1 and I2 filters. Using images on +564 day as a reference, Chen et al. (2022) made difference images for the first three epochs, on which they measured the fluxes of SN 2018bsz. We checked whether our measurements using WISE data are consistent with these

Table B1. WISE photometry of the 11 SLSNe.

MJD	Phase	W1		W2	
		flux μ Jy	mag Vega	flux μ Jy	mag Vega
PS15br					
57175.4	+78.2	61(9)	16.77(0.17)	46(21)	>16.1
57367.9	+253.1	25(10)	>17.5	36(24)	>16.0
57534.2	+404.1	45(10)	17.08(0.23)	39(18)	>16.2
57732.2	+583.9	57(11)	16.83(0.21)	85(23)	15.77(0.29)
57894.7	+731.5	62(10)	16.74(0.17)	67(19)	16.03(0.31)
58097.7	+915.9	38(10)	17.27(0.28)	43(25)	>15.9
58255.0	+1058.8	20(11)	>17.4	30(21)	>16.1
58463.4	+1248.0	26(11)	>17.4	56(24)	>15.9
58622.2	+1392.3	10(12)	>17.4	13(23)	>16.0
SN2015bn					
57180.7	+70.7	57(10)	16.84(0.18)	60(20)	16.15(0.36)
57373.1	+243.4	15(11)	>17.5	40(20)	>16.2
57539.6	+393.0	22(10)	>17.5	59(22)	>16.1
57739.5	+572.5	16(10)	>17.5	30(23)	>16.0
57900.1	+716.6	11(11)	>17.5	28(21)	>16.1
LSQ15abl					
57154.6	+17.1	78(14)	16.50(0.19)	22(22)	>16.0
57348.2	+195.2	51(15)	16.95(0.32)	28(22)	>16.1
57517.4	+350.8	31(15)	>17.1	2(23)	>16.0
57713.7	+531.5	11(12)	>17.3	30(19)	>16.2
57875.4	+680.2	-17(14)	>17.2	35(19)	>16.2
SN2016eay					
57524.5	-15.4	27(9)	17.64(0.36)	23(18)	>16.2
57724.4	+166.2	34(11)	17.41(0.34)	-2(25)	>15.9
57886.4	+313.3	11(10)	>17.5	-5(23)	>16.0
58092.0	+499.9	-1(11)	>17.4	38(23)	>16.0
58246.9	+640.6	-10(10)	>17.5	13(23)	>16.0
SN2017ens					
57908.6	-13.9	13(10)	>17.5	19(25)	>15.9
58111.1	+168.8	31(10)	17.48(0.35)	11(23)	>16.0
58270.5	+312.6	78(9)	16.50(0.13)	34(20)	>16.1
58475.3	+497.3	73(10)	16.56(0.15)	92(20)	15.67(0.24)
58634.7	+641.1	71(9)	16.60(0.13)	86(19)	15.76(0.24)
58842.3	+828.3	58(11)	16.82(0.21)	37(24)	>15.9
59000.4	+970.9	41(9)	17.19(0.22)	55(20)	>16.1
SN2017egm					
58067.5	+137.5	81(19)	16.46(0.26)	166(30)	15.04(0.20)
58227.3	+292.5	81(19)	16.45(0.26)	105(32)	15.54(0.33)
58433.1	+492.2	69(23)	>16.6	110(31)	15.48(0.30)
58589.3	+643.8	12(20)	>16.8	-4(33)	>15.6
58797.4	+845.7	14(19)	>16.8	-4(32)	>15.6
58954.9	+998.5	-11(20)	>16.8	26(34)	>15.6
SN2017err					
57894.9	-36.2	-4(9)	>17.7	-6(19)	>16.2
58097.9	+147.2	16(8)	>17.8	19(23)	>16.0
58255.3	+289.3	40(8)	17.22(0.22)	32(19)	>16.2
58463.6	+477.5	44(12)	17.11(0.28)	66(23)	>16.0
58622.4	+620.9	30(10)	>17.5	51(20)	>16.2
58827.9	+806.6	10(11)	>17.5	7(22)	>16.0
SN2017gci					
58035.5	+41.6	42(10)	17.17(0.25)	60(18)	16.15(0.33)
58191.5	+185.0	31(9)	17.48(0.32)	82(18)	15.81(0.23)
58401.2	+377.9	17(11)	>17.5	20(19)	>16.2
58557.1	+521.3	-5(7)	>17.9	-3(15)	>16.4
58765.4	+712.9	15(11)	>17.5	-31(22)	>16.1
SN2018bgv					
58228.0	-23.4	2(7)	>18.0	-39(15)	>16.5
58434.6	+168.1	18(8)	>17.7	21(15)	>16.4
58592.3	+314.1	-2(7)	>18.0	-4(15)	>16.4
58801.9	+508.3	4(8)	>17.8	-19(19)	>16.2
58956.4	+651.4	3(7)	>17.9	4(16)	>16.4
SN2018bsz					
58336.6	+67.3	552(24)	14.37(0.05)	404(28)	14.07(0.08)
58539.3	+264.7	208(22)	15.43(0.11)	385(28)	14.12(0.08)
58702.1	+423.3	33(22)	>16.7	70(29)	>15.7
58904.9	+620.8	23(23)	>16.6	-55(27)	>15.8
59067.9	+779.5	-7(21)	>16.7	-17(30)	>15.7
SN2018hti					
58508.2	+41.1	300(11)	15.03(0.04)	177(21)	14.97(0.13)
58715.5	+236.4	75(13)	16.54(0.18)	75(26)	>15.9
58872.4	+384.3	39(10)	17.25(0.27)	68(19)	16.01(0.31)
59080.7	+580.6	21(10)	>17.6	29(22)	>16.0

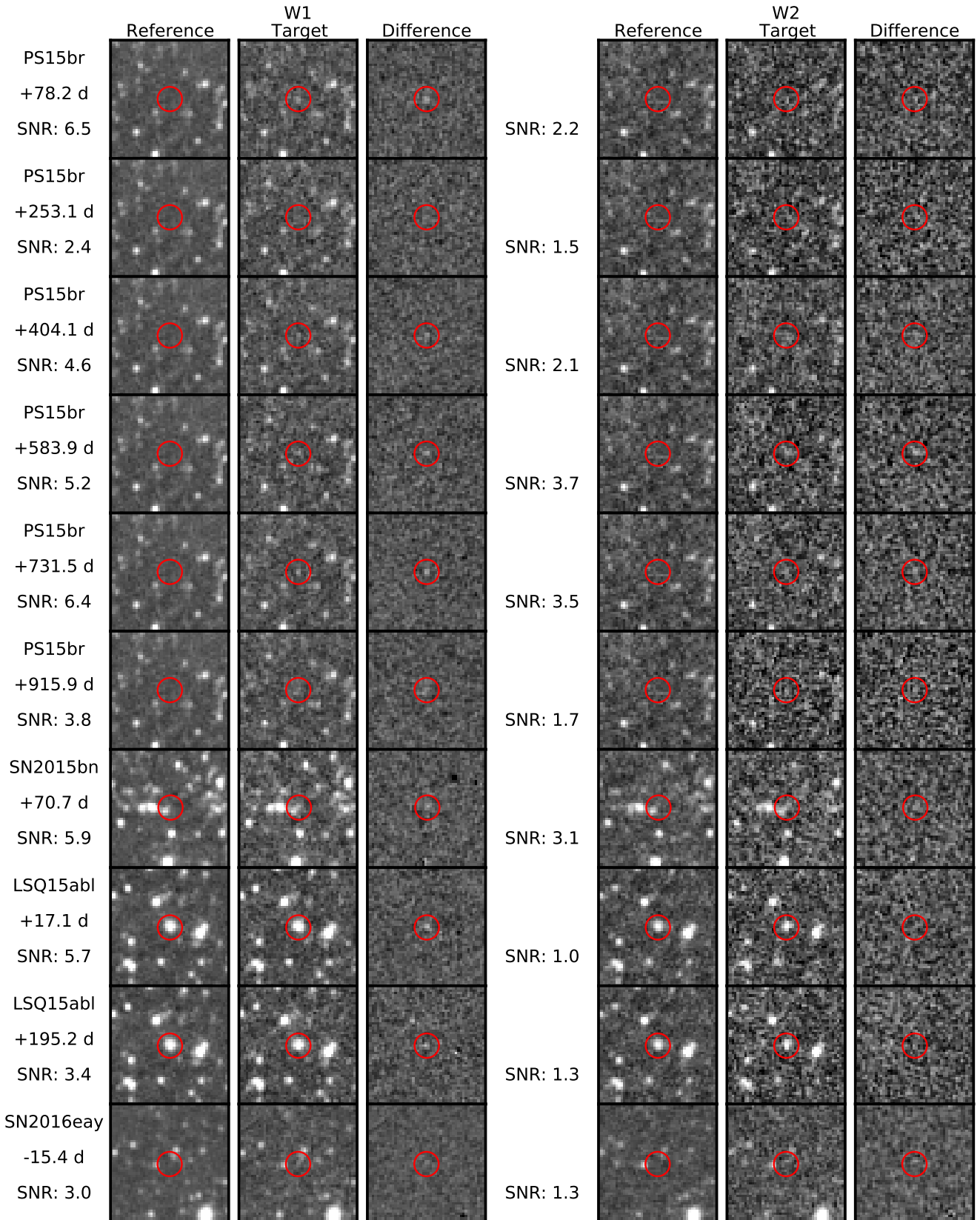


Figure B1. The reference, target, and difference images in the W1 band (left) and W2 band (right). Red circles show the target positions. The object name, the phase, and the signal to noise ratio are labeled.

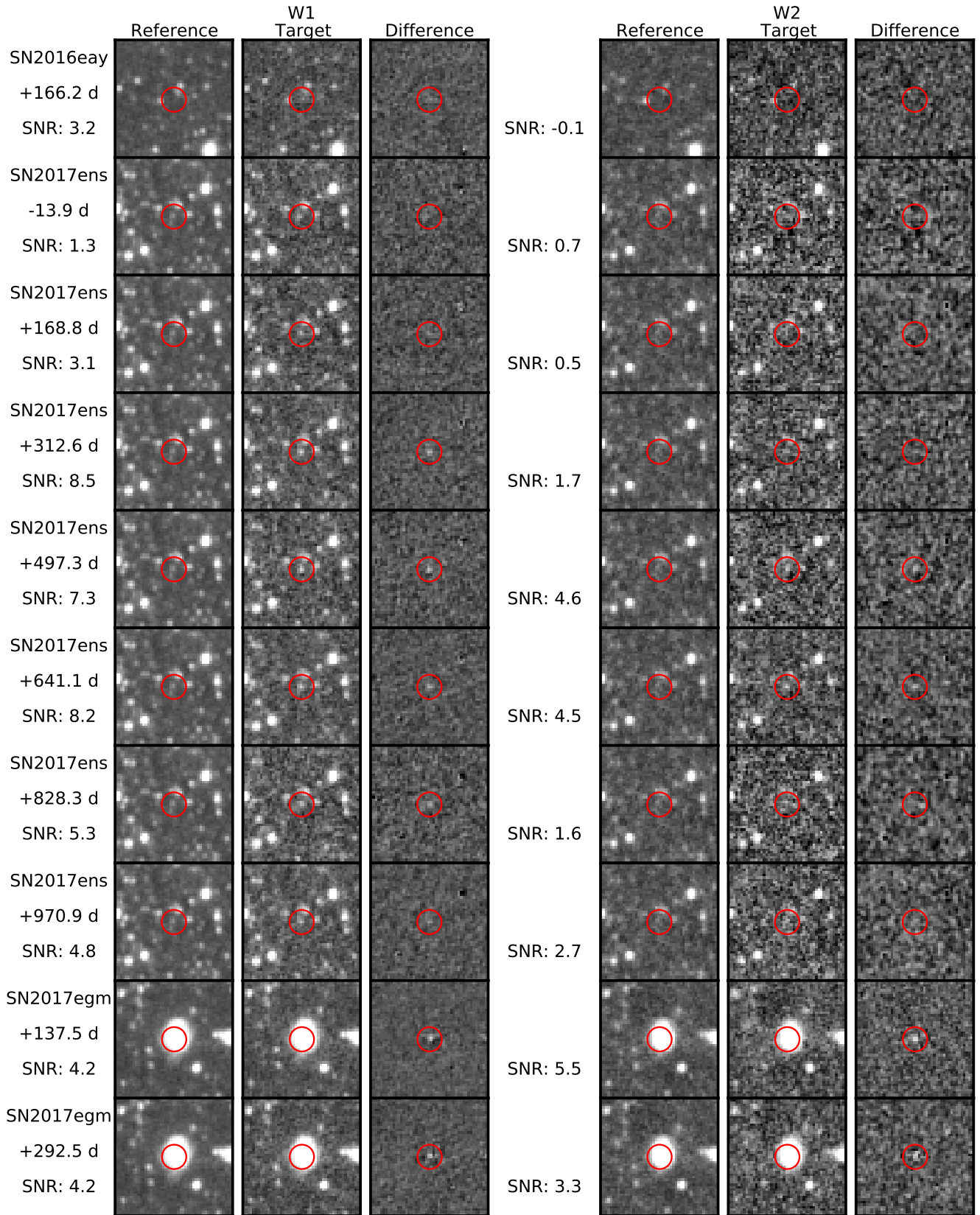


Figure B2. Continued to Fig. B.

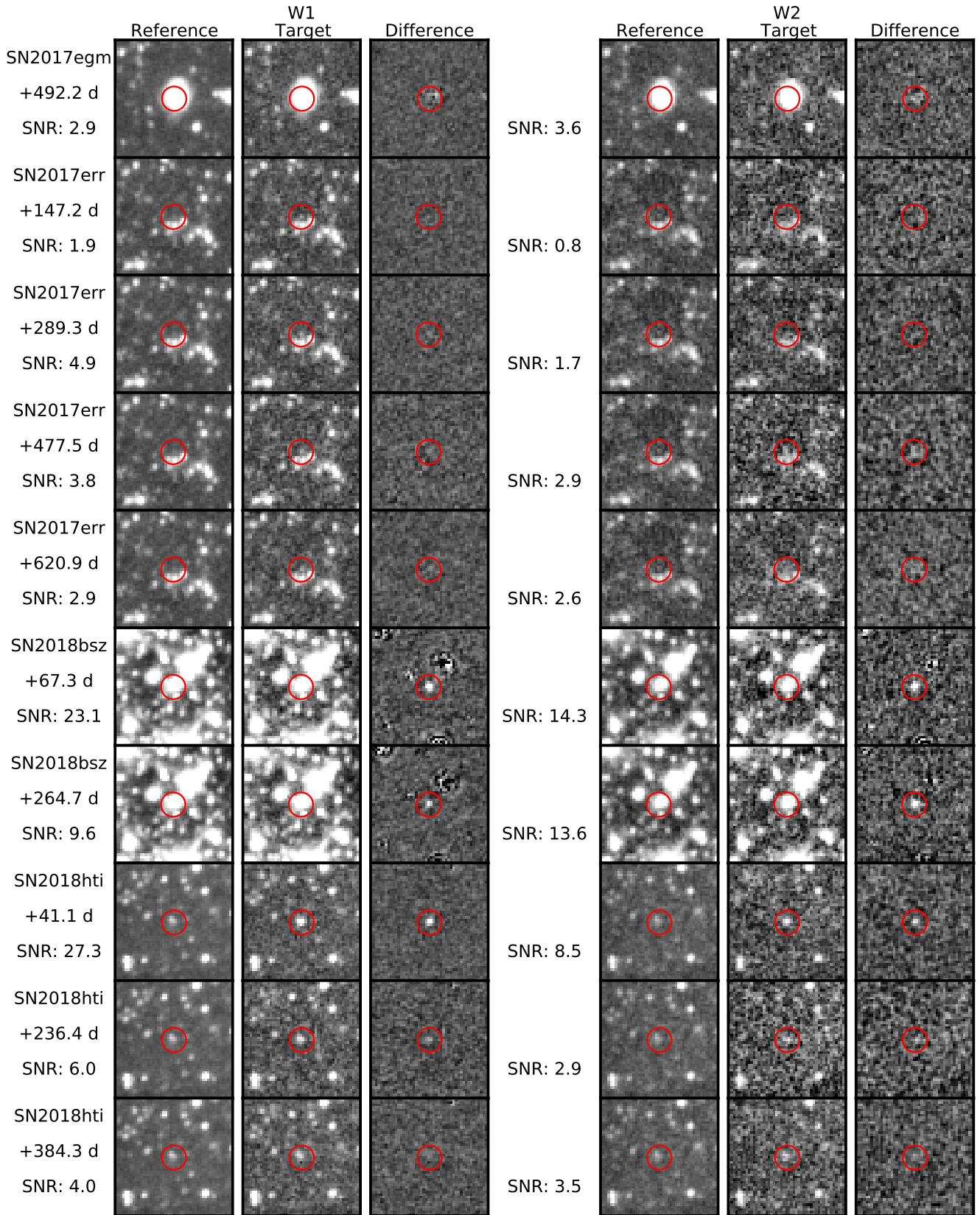


Figure B3. Continued to Fig. B.

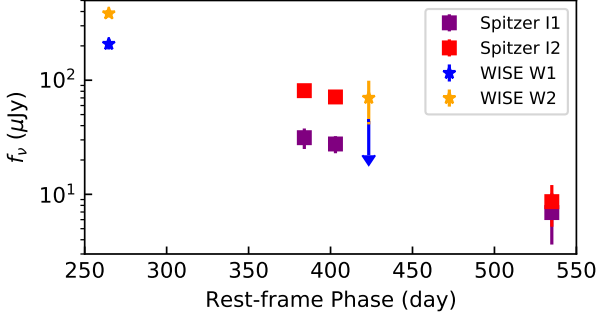


Figure C1. : A comparison between the WISE and Spitzer photometries of SN 2018bsz.

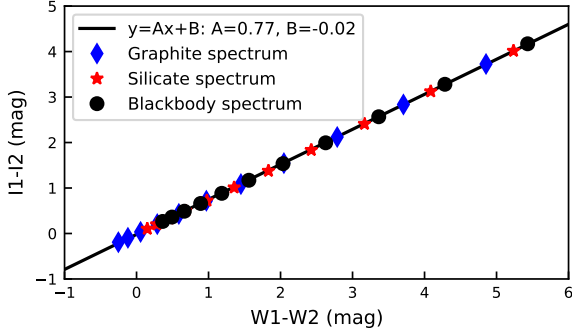


Figure D1. : The $W1 - W2$ and $I1 - I2$ colors for spectra of blackbodies and optically thin dust with temperatures between 200 and 2000 K, and the best-fitting linear function.

measurements using Spitzer data. As can be seen from Fig. C, the two sets of measurements agree with each other.

APPENDIX D: RELATION BETWEEN WISE $W1 - W2$ AND SPITZER $I1 - I2$ COLORS

In order to compare the SLSN $W1 - W2$ color with the $I1 - I2$ color of normal SNe measured by Spitzer in the literature, we search for the conversion between $W1 - W2$ and $I1 - I2$ colors for dust spectra. We assumed a series of blackbody spectra with temperatures between 200 and 2000 K in 0.1 dex step, and calculated the synthetic magnitudes⁵ in WISE and Spitzer bands, and hence the MIR colors. We also calculated MIR colors for spectra of optically thin dust assuming graphite and silicate dust. As can be seen in Fig. D, the $W1 - W2$ color and the $I1 - I2$ color are linearly correlated for typical dust spectra. By fitting these data points with a linear function, we obtained equation (1) as shown in the black line.

⁵ We used the response curves of Spitzer filters from <https://irsa.ipac.caltech.edu/data/SPITZER/docs/irac> and those of WISE filters from <https://wise2.ipac.caltech.edu/docs/release/prelim/expsub>

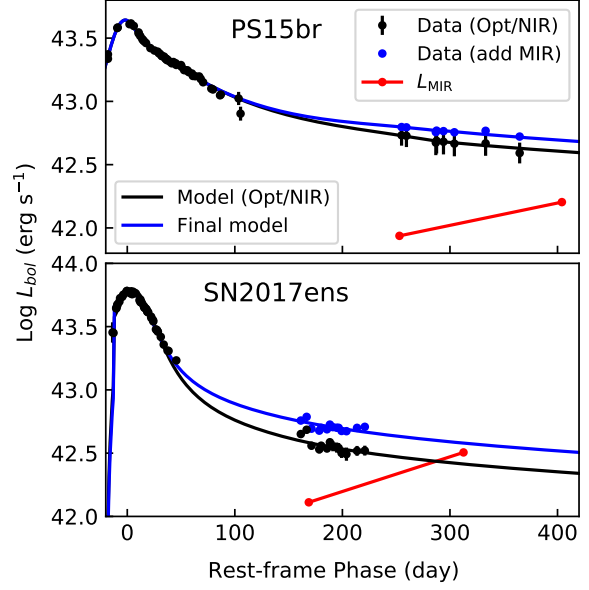


Figure E1. : The bolometric LC and models for PS15br and SN 2017ens.

APPENDIX E: THE BOLOMETRIC LIGHT CURVES OF PS15BR AND SN 2017ENS

Insera et al. (2018) and Chen et al. (2018) have calculated the bolometric LCs for PS15br and SN 2017ens, respectively. However, they only considered UV, optical, and NIR emissions in their calculations. By considering the MIR emission, we recalculated the bolometric LCs for PS15br and SN 2017ens following a method used in Chen et al. (2022). We collected the LC data from the literature, which are shown in Fig. E in black points. The optical/NIR data are available until +365d for PS15br and until +221d for SN 2017ens. We calculated MIR luminosities (red points) using the $W1$ -band luminosity assuming a $C_B(W1) = 1.5$. We found that MIR emission accounted for more than 10% of the total luminosity after +150d. Therefore, for data points after that, we computed MIR luminosity by interpolating the observed data assuming an exponential function (red lines), and summed the optical/NIR luminosity and the MIR luminosity to obtain the bolometric luminosity (blue points).

The bolometric LCs of the two SLSNe decrease slowly in the late time. This is likely because the heating of the CSM interaction dominates. Therefore, we extrapolated the measured bolometric LC to later phases using a CSM interaction model. Following Chen et al. (2018), we assumed a function of $L_{bol} = L_{int,1}(t/1 \text{ s})^{-3/5}$ for this model. In addition, we concatenated the early-time data simply using cubic spline functions. The final results are shown in blue lines.

APPENDIX F: THE BOLOMETRIC CORRECTIONS

We calculated the bolometric corrections C_B in the $W1$ -band for different dust temperatures T_d using equation (3) by assuming dust spectra expressed as equation (2). The dust spectra were shifted to the observer's frame according to

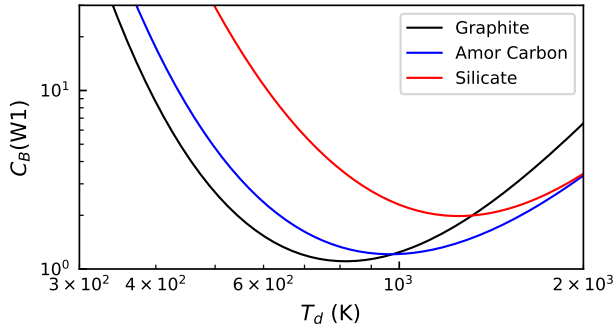


Figure F1. The bolometric correction in the W1 band as a function of T_d at $z = 0.105$.

Table F1. Minimum C_B in the W1 band at $z = 0.105$

Dust	minimum C_B
Graphite	1.10 (810 K)
Amor Carbon	1.21 (970 K)
Silicate	1.98 (1250 K)

$z = 0.105$, since PS15br, SN 2017ens and SN 2017err are at redshifts between 0.101 and 0.109. The results, assuming three different dust compositions, are displayed in Fig. F. The minimum values of C_B and the corresponding T_d are listed in Tab. F1.

This paper has been typeset from a $\text{\TeX}/\text{\LaTeX}$ file prepared by the author.